frontiers | Frontiers in Nanotechnology

TYPE Original Research
PUBLISHED 11 November 2022
DOI 10.3389/fnano.2022.1049599

OPEN ACCESS

EDITED BY
Marlus Chorilli,
São Paulo State University, Brazil

REVIEWED BY
Liliana Verestiuc,
Grigore T. Popa University of Medicine and Pharmacy, Romania
Thi Thai Thanh Hoang,
Emory University, United States

*CORRESPONDENCE
Eliana Martins Lima,
emlima@ufg.br

SPECIALTY SECTION
This article was submitted to Biomedical Nanotechnology, a section of the journal Frontiers in Nanotechnology

RECEIVED 20 September 2022
ACCEPTED 25 October 2022
PUBLISHED 11 November 2022

CITATION
Vasconcelos MO, Silva LAD, Sousa-Junior AA, dos Santos TRM, da Silva CA, Valadares MC and Lima EM (2022), Lidocaine- and chloramphenicol-loaded nanoparticles embedded in a chitosan/hyaluronic acid/glycerol matrix: Drug-eluting biomembranes with potential for guided tissue regeneration.
Front. Nanotechnol. 4:1049599.
doi: 10.3389/fnano.2022.1049599

Lidocaine- and chloramphenicol-loaded nanoparticles embedded in a chitosan/hyaluronic acid/glycerol matrix: Drug-eluting biomembranes with potential for guided tissue regeneration

Mariana Oliveira Vasconcelos[1], Luís Antônio Dantas Silva[1], Ailton Antonio Sousa-Junior[1], Thaís Rosa Marques dos Santos[2], Carla Afonso da Silva[3], Marize Campos Valadares[2] and Eliana Martins Lima[1]*

[1]FarmaTec–Laboratory of Pharmaceutical Technology, School of Pharmacy, Federal University of Goiás, Goiânia, Brazil, [2]ToxIn–Laboratory of Education and Research in In Vitro Toxicology, School of Pharmacy, Federal University of Goiás, Goiânia, Brazil, [3]Lafebim–Laboratory of Anaerobes, Phenotyping and Molecular Biology, Institute of Tropical Pathology and Public Health, Federal University of Goiás, Goiânia, Brazil

Guided tissue regeneration (GTR) is a dentistry technique based on the use of polymeric biomembranes as physical barriers for selective cell exclusion, directing the growth of gingival tissue, bone tissue, and periodontal ligaments in a region previously affected by periodontitis. Postoperative pain and microbial infection constitute, however, two major challenges to be tackled right after implantation. To address these challenges, we prepared and characterized eight chitosan/hyaluronic acid/glycerol (CS/HA/GL) bioresorbable membranes embedded with lidocaine- and chloramphenicol-loaded polycaprolactone nanoparticles (LDNP and CHNP, respectively), combining the local anesthetic effects of lidocaine with the antibacterial effects of chloramphenicol. The formulations were prepared with varying amounts of CS, HA, GL, LDNP, and CHNP. As a plasticizing agent, GL could modulate the samples mechanical properties such as thickness, morphology, tensile strength, elongation at break, as well as swelling and degradation in simulated saliva. Two samples exhibited greater resistance to biodegradation and were selected for further studies. Their drug release profiles indicated that LDNP and CHNP first detach from the membrane matrix, and a zeroth order drug release kinetics from the detached NPs dominates the overall process thereafter, with lidocaine being released 3 times faster than chloramphenicol, in a controlled and sustained rate over time. Drug encapsulation efficiency was such that optimal samples exhibited bactericidal activity (inhibition halos) against gram-positive *S. aureus* and gram-negative *A. actinomycetemcomitans* strains similar to that observed for free

chloramphenicol. Finally, one of these samples showed no intrinsic toxicity against healthy mammalian model cells (99% viability for the unloaded membrane; 80% viability for the fully LDNP- and CHNP-loaded membrane), and may now be further optimized as a drug-eluting biomembrane with potential for GTR.

KEYWORDS

lidocaine, nanoparticles, chitosan, hyaluronic acid, glycerol, guided tissue regeneration, antibacterial activity, bioresorbable membranes

1 Introduction

Guided tissue regeneration (GTR) is a dentistry technique based on the use of polymeric biomembranes as physical barriers for selective cell exclusion, directing the growth of gingival tissue, bone tissue, and periodontal ligaments in a region previously affected by periodontitis (Castillo Dalí and Torres Lagares, 2016; Zhang et al., 2016; Bhavsar et al., 2018). Conventionally, the basic requirements for GTR membranes are good flexibility and biocompatibility, as well as suitable biodegradation profile and physicochemical/mechanical properties (Sgorla et al., 2016; Osathanon et al., 2017; Khorsand et al., 2019).

Chitosan (CS) and hyaluronic acid (HA) are among the polymers of interest for the development of membranes used in periodontal GTR (Battistella et al., 2011; Dahiya and Kamal, 2013). Derived from chitin, CS is one of the most abundant biopolymers in nature. HA, in turn, is a hydrophilic polysaccharide naturally present in the extracellular matrix. Both are biocompatible polymers, adequate for use in periodontal GTR membranes (Ballini et al., 2009; Zhang et al., 2011). Glycerol (GL) is widely applied in the pharmaceutical, cosmetic and food industries, generally as a plasticizing agent. Indeed, when introduced in polymeric matrices, GL can modulate their mechanical properties, consequently favoring mobility/diffusivity within the matrix, among other effects (Fundo et al., 2014; Wang and Jing, 2017).

The use of these biomembranes as drug-eluting devices is a more recent approach (Gupta and Ravi Kumar, 2000; Vahabi and Mardanifar, 2014). Drugs may be directly dispersed in the membrane matrix, or otherwise entrapped in nanoparticles, and then embedded in the matrix. The advantages of the latter strategy are the reduction of the drug toxicity and a prolonged drug release profile (Thein-Han and Stevens, 2004; Anisha et al., 2013; Ma et al., 2014; Sanchez-Rexach et al., 2018). Indeed, drug-loaded nanoparticles can physicochemically bind to the biomembranes and to local tissues, which not only prevents their rapid clearance, increasing their residence time in the oral mucosa, but also contributes to the sustained release of their cargo (Patel et al., 2011; Pramod et al., 2016). However, a growing number of studies propose drug delivery systems based either on inorganic materials (Prado-Prone et al., 2020; Yin et al., 2020), or on more complex fabrication protocols, such as uniaxial or coaxial electrospinning (Shi et al., 2019; Xu et al., 2020).

In this study, we prepare and characterize drug-eluting bioresorbable membranes for GTR, aiming to achieve sustained anesthetic and antimicrobial effects, thus addressing both postoperative pain and eventual sources of infection (Thein-Han and Stevens, 2004; Aravamudhan et al., 2013; Kiruthika et al., 2015). The novelty of the work consists of embedding two types of drug-loaded nanoparticles in biomembranes usually applied for GTR. Indeed, drug-free biomembranes have been traditionally used for GTR, with anesthetics and antibiotics eventually administered separately, either systemic or by local injection (Sgorla et al., 2016; Osathanon et al., 2017; Khorsand et al., 2019). Drug-eluting biomembranes have been developed as alternatives, yet with drugs either directly dispersed throughout the matrix, or loaded in electrospun nanofibers (Gupta and Ravi Kumar, 2000; Vahabi and Mardanifar, 2014). Herein, we chose drug-loaded nanoparticles instead, since they are easier to prepare than electrospun nanofibers, especially when a dual regime (anesthetic and antibiotic) is desired in a controlled and sustainable manner.

We prepared drug-eluting biomembranes consisting of a CS/HA/GL matrix embedding lidocaine- and chloramphenicol-loaded polycaprolactone nanoparticles (LDNP and CHNP, respectively). Lidocaine works as a fast-acting local anesthetic, while chloramphenicol acts as broad-spectrum antibiotic. The fabrication protocols employed are rather simple, with the CS/HA/GL biomembranes being prepared by casting, and the drug-loaded nanoparticles being prepared by nanoprecipitation. The physicochemical/mechanical properties, degradation, swelling and drug release profiles, as well as antibacterial activity and biocompatibility of different samples were thoroughly examined, leading to the development of an optimal drug-eluting system with potential for periodontal GTR.

2 Materials and methods

2.1 Materials

Lidocaine, chloramphenicol, poly(ε-caprolactone), Pluronic F-127, chitosan (low molecular weight), hyaluronic acid, acetic acid, acetone, acetonitrile, trifluoroacetic acid, methanol, sodium

hydroxide (NaOH), phosphate buffer saline (PBS), ethylene oxide, DMEM, penicillin, streptomycin, inactivated fetal bovine serum, and trypsin-EDTA, were purchased from Sigma Aldrich, United States. Miglyol® 812 N was obtained from Sasol, Germany. Soybean phosphatidylcholine was acquired from Lipoid, Germany. Glycerol was bought from Labsynth, Brazil. Mueller-Hinton agar (MHA) was purchased from Acromed, Brazil. Defibrinated horse blood was obtained at the Cavalry Battalion of the Military Police of Goiás, Brazil. The cell viability kit Live/Dead Cell (calcein/EthD-1) was provided by Life Technologies, United States. Water was obtained from a Milli-Q system commercialized by Millipore, United States. All other chemicals were of analytical grade.

2.2 Preparation and characterization of lidocaine- and chloramphenicol-loaded nanoparticles

Lidocaine- and chloramphenicol-loaded nanoparticles (LDNP and CHNP) were prepared separately, by nanoprecipitation (Fessi et al., 1989). Briefly, 6 mg of lidocaine (or chloramphenicol) were dissolved in 6 ml of acetone, along with 50 mg of poly(ε-caprolactone) (PCL), 150 µg Miglyol® 812 N, and 50 mg of soybean phosphatidylcholine, to form the organic phase. The aqueous phase, on the other hand, contained 100 mg of Pluronic F-127 in 12 ml of ultrapure water. The organic phase was then poured into the aqueous phase, and solvents were removed under controlled pressure in a rotary evaporator (IKA) at 40°C, leading to a final volume of 6 ml (and therefore, 1 mg of lidocaine or chloramphenicol per mL).

2.2.1 Size and polydispersion

Nanoparticles mean hydrodynamic diameter and polydispersity index (PdI) were determined *via* dynamic light scattering (DLS), using a ZetaSizer Nano S (Malvern Panalytical, United Kingdom). Readings were performed in triplicate.

2.2.2 Drug analytical quantitation

Drug quantitation was performed *via* high-performance liquid chromatography (HPLC), using an Agilent 1200 Infinity Series HPLC (Agilent Technologies, Lake Forest, California) equipped with a UV-Vis detector. The Zorbax-Eclipse-C18 chromatographic column (150 mm × 4.6 mm) was kept at 35 °C during the runs. The mobile phase consisted of acetonitrile (ACN) and acidified water (trifluoroacetic acid, TFA, 0.1%) at a volumetric ratio of 75:25 (ACN:H_2O). The sample injection volume was 10 µL, the flow rate was set to 1 ml/min, and the detection wavelengths were 230 nm for lidocaine and 360 nm for chloramphenicol (Iqbal et al., 2006; Al-Rimawi and Kharoaf, 2011; Ramos Campos et al., 2013; Bhusal et al., 2017).

2.2.3 Encapsulation efficiency

Drug encapsulation efficiency (EE) was calculated as follows:

$$EE\ [\%] = \frac{\text{total drug} - \text{free drug}}{\text{total drug}} \times 100 \quad (1)$$

To quantitate the free drug, an aliquot of the given colloidal dispersion was placed in a 20-kDa Vivaspin® centrifugal filtration device (Sigma-Aldrich, St. Louis, MO, United States), and centrifuged at 5,000 g for 30 min. Then, 100 µl of the resulting filtrate was diluted in 900 µl of methanol for HPLC quantitation. Meanwhile, to quantitate the total drug, 100-µl aliquots of the selected colloid were first added to 900 µl of methanol for extraction, and then centrifuged at 14,500 rpm for 20 min to separate the total drug from the polymeric content. Supernatants were then collected for HPLC quantitation.

2.2.4 Drug release from lidocaine- and chloramphenicol-loaded nanoparticles

In vitro drug release assays were accomplished by diffusion through dialysis membranes. The donor medium consisted of 1.6 ml of the assessed colloid, and the receptor medium consisted of 20 ml of artificial saliva, prepared as previously reported (Ionta et al., 2014), with sink conditions satisfied. The system was kept under orbital shaking at 50 rpm and 37°C for up to 120 h. Aliquots (200 µl) were withdrawn from the receptor medium at pre-established times (1, 3, 6, 9, 12, 24, 48, 96, and 120 h) and replaced by the same volume of fresh medium at each sampling. Each aliquot was then diluted in 800 µl of methanol for drug extraction, followed by drug quantitation *via* HPLC.

2.3 Preparation and characterization of drug-eluting chitosan/hyaluronic acid biomembranes

Eight different biomembranes were prepared with varying compositions of chitosan (CS), hyaluronic acid (HA), glycerol (GL), acetic acid, LDNP, and CHNP, as described in Table 1. Noteworthy, Group 1_{35} membranes were designed with overall lower CS, HA, GL, acetic acid, and drug contents compared to Group 2_{100} membranes.

The sample names are $MX_{CS|HA|GL}$, where X stands both for the membrane group and for the volume (in ml) of both LDNP and CHNP colloidal dispersions used in the sample preparation. Hence, Group 1_{35} membranes were prepared with 1 ml of both LDNP and CHNP, whereas Group 2_{100} membranes were prepared with 2 ml of both LDNP and CHNP.

Additionally, the subscripts CS and HA stand for the proportional amount (in mg) of chitosan and hyaluronic acid used in the sample preparation, while the subscript GL stands for

TABLE 1 Biomembranes: Designed composition.

	Group 1_{35}				Group 2_{100}			
	$M1_{211}$	$M1_{215}$	$M1_{2.21}$	$M1_{2.25}$	$M2_{211}$	$M2_{215}$	$M2_{2.21}$	$M2_{2.25}$
CS [mg]	70	70	70	70	200	200	200	200
HA [mg]	35	35	7	7	100	100	20	20
Glycerol [μL]	35	175	35	175	100	500	100	500
Acetic acid [μL]	100	100	100	100	300	300	300	300
$LDNP_{[1\ mg/mL]}$ [mL]	1	1	1	1	2	2	2	2
$CHNP_{[1\ mg/mL]}$ [mL]	1	1	1	1	2	2	2	2

M, membrane; **CS**, chitosan; **HA**, hyaluronic acid; **LDNP**, lidocaine-loaded nanoparticles; **CHNP**, chloramphenicol-loaded nanoparticles. The subscript [1 mg/ml] corresponds to the designed lidocaine or chloramphenicol concentration.

the proportional volume (in μl) of glycerol. The corresponding group subscript is a multiplication factor that yields the actual amount of CS, HA, and GL used.

For instance, sample $M2_{211}$ belongs to Group 2_{100} and was then prepared with 2 ml of both LDNP and CHNP, 2 × 100 = 200 mg of CS, 1 × 100 = 100 mg of HA, and 1 × 100 = 100 μl of GL. On the other hand, sample $M1_{2.21}$ belongs to Group 1_{35} and was then prepared with 1 ml of both LDNP and CHNP, 2 × 35 = 70 mg of CS, 0.2 × 35 = 7 mg of HA, and 1 × 35 = 35 μl of GL.

All membranes were prepared by casting, as previously described in the literature (Yan et al., 2000; Xu et al., 2007; Contri et al., 2010; Yao and Wu, 2011), yet with some modifications. Briefly, HA was first dispersed in water. Then, CS, GL, acetic acid, LDNP and CHNP were added, and the mixture was left under magnetic stirring at 25°C for 24 h. Next, the resulting dispersions were poured into plastic Petri dishes (60 mm × 15 mm) and kept under 37°C in an air-circulating oven for 24 h. The resulting membranes were then washed with distilled water and NaOH solution (1% w/v), and, finally, left for drying under 37 °C in an air-circulating oven for 1 h.

2.3.1 Thickness and morphology

Membrane thickness was determined with a digital caliper. Measurements were taken in triplicates at five different points along the length, and thickness was calculated as the resulting mean value.

Surface and cross-sectional morphology were analyzed *via* FESEM (Field Emission Scanning Electron Microscopy, JSM-7100F, JEOL, United States). Before imaging, the membranes were first cut in rectangles (2 cm × 1 cm) and then coated with a thin layer of gold. Micrographs were taken at ×3,000 magnification at room temperature.

2.3.2 Tensile strength and elongation at break

Tensile strength (TS) and elongation at break (EB) were obtained using a TA-XT Plus Texture Analyzer (Stable Micro Systems, Surrey, England). The membranes were cut in strips 1 cm wide and 5 cm long and attached to the lower and upper ends of the analytical probe, which were initially distant of 3.5 cm. The elongation rate was set at 10 mm/s, with a load cell capacity of 50 kg. Measurements were taken in triplicates at 25°C.

2.3.3 *In vitro* degradation profile

Degradation rate in simulated saliva was also evaluated. The membranes were first cut in rectangles (2 cm × 1 cm), then weighed, and incubated in 10 ml of artificial saliva at 37°C for 1, 7, 14, 21, and 28 days. At the end of each sampling time, the membranes were removed from the incubation medium and placed in an oven at 37°C for drying and then weighing. All measurements were taken in triplicates. The weight loss (WL) was calculated as follows:

$$\mathrm{WL}\ [\%] = \frac{W_0 - W_d}{W_0} \times 100 \tag{2}$$

where W_0 represents the membrane initial dry weight, and W_d represents its dry weight after incubation in simulated saliva at a given sampling time.

2.3.4 Swelling profile

Similarly, swelling in simulated saliva was also assessed. The membranes were first cut in rectangles (2 cm × 1 cm), then weighed, and incubated in 5 ml of artificial saliva at 25°C for 0.25, 0.5, 1, 3, 6, 12, and 24 h. At the end of each sampling time, the superficial excess of saliva was carefully wiped off with absorbent paper, and the membranes wet weight was determined. All measurements were taken in triplicates. The swelling index (SI) was calculated as follows:

$$\mathrm{SI}\ [\%] = \frac{W_w - W_0}{W_0} \times 100 \tag{3}$$

where W_0 represents the membrane initial dry weight, and W_w represents its wet weight after incubation in simulated saliva at a given sampling time.

2.3.5 Drug release from biomembranes embedded with lidocaine- and chloramphenicol-loaded nanoparticles

Membranes were immersed in 25 or 50 ml of artificial saliva so that sink conditions were satisfied for both drugs. Samples were kept under orbital shaking at 150 rpm and 37°C. Aliquots (1 ml) were withdrawn at pre-established times (1, 3, 6, 9, 12, and 24 h) and replaced by the same volume of fresh medium at each sampling. Each aliquot was then diluted in methanol (1:4 v/v) for drug extraction, followed by drug quantitation *via* HPLC.

2.3.6 Antibacterial activity

Antibacterial activity was assessed by diffusion in Mueller-Hinton agar (MHA) and in Mueller-Hinton agar plus 5% v/v defibrinated horse blood (MHB). Assays were conducted against the gram-positive *Staphylococcus aureus* (ATCC 25923) and the gram-negative *Aggregatibacter actinomycetemcomitans* (FDC Y4) (Tihan et al., 2015; Szafrański et al., 2017). Bacterial suspensions were obtained in 0.85% saline at 0.5 McFarland turbidity. *S. aureus* was seeded in MHA, and *A. actinomycetemcomitans* was seeded in MHB. Membranes were first sterilized using ethylene oxide, then placed on Petri plates, and incubated with the bacterial suspensions at 37°C for 24 h. Plates with *S. aureus* were kept under aerobiosis, while plates with *A. actinomycetemcomitans* were kept under microaerophilic conditions. Assays were performed in triplicates, and readings were taken by measuring the halo size in mm. The interpretation of halo sizes was that of the Clinical Laboratory Standards Institute (CLSI) for *S. aureus*. For *A. actinomycetemcomitans*, since the CLSI does not define a reference halo size for chloramphenicol, the interpretation was instead based on the presence/absence of the inhibition halo.

2.3.7 Biocompatibility

Biocompatibility assays were performed on 3T3 fibroblasts (ATCC CRL-1658) using the cell viability kit Live/Dead Cell (calcein/EthD-1). The 3T3 murine lineage is a common model of normal healthy mammalian cells (Henklewska et al., 2021). Cells were cultured in DMEM, supplemented with 10% v/v inactivated fetal bovine serum and 1% v/v penicillin/streptomycin. Culture bottles (75 cm^2) were kept at 37°C, under 5% CO_2 atmosphere and controlled humidity. Culture medium was renewed every other day until 90% confluence. For cell detachment, 0.25%–0.03% v/v trypsin-EDTA was used.

Considering their optimal degradation profiles, $M1_{2.21}$ and $M2_{211}$ were selected for the biocompatibility assay. Membranes were first sterilized using ethylene oxide, then cut in rectangles (2 cm × 1 cm), placed in the center of 35 mm × 15 mm plates previously seeded with 3T3 monolayers (approximately 5×10^4 cells) and incubated for 24 h. Next, the membranes were removed from the plates, and the cells were washed with PBS. Following the manufacturer's protocol, 1 ml of calcein/EthD-1 solution was used for staining. Viability results were obtained *via* fluorescence microscopy (DMI 4000 B, Leica Microsystems, Bannockburn, United States). Calcein was excited at 488 nm and the corresponding fluorescence was detected within 491–545 nm (L5 filter, green, stain for live cells). EthD-1 was excited at 568 nm and the corresponding fluorescence was detected within 590–685 nm (N21 filter, red, stain for dead cells).

Cell viabilities were calculated as follows:

$$\text{Viability } [\%] = \frac{\text{MFI}_{\text{green}}}{\text{MFI}_{\text{green}} + \text{MFI}_{\text{red}}} \times 100 \quad (4)$$

where MFI stands for mean fluorescence intensity. Mean values were calculated over ten equally sized random areas over the corresponding image, neglecting the background fluorescence.

TABLE 2 Characterization of LDNP and CHNP.

	LDNP	CHNP
D_H [nm]	212 ± 2	208 ± 2
PdI	0.26 ± 0.04	0.23 ± 0.01
EE [%]	77 ± 4	83 ± 5
Encapsulated drug [mg]	4.6 ± 0.2	5.0 ± 0.3

LDNP, lidocaine-loaded nanoparticles; **CHNP**, chloramphenicol-loaded nanoparticles; **D_H**, mean hydrodynamic diameter; **PdI**, polydispersity index; **EE**, encapsulation efficiency.

2.4 Statistical analysis

Measurements were expressed as mean value ± SD. Statistical analyses were performed in GraphPad Prism 5 *via* analysis of variance (ANOVA) followed by Tukey test or *via* student's T-test. Statistically significant differences were considered for $p < 5\%$.

3 Results

3.1 Preparation and characterization of lidocaine- and chloramphenicol-loaded nanoparticles

Both lidocaine- and chloramphenicol-loaded polymeric nanoparticles (LDNP and CHNP) presented mean hydrodynamic diameters of approximately 200 nm, with PdI within 0.2–0.3, suggesting low polydispersity (Table 2). LDNP and CHNP reduced size favors their embedding in polymeric matrices, enabling drug-elution in the vicinity of the site where the biomembrane was implanted—an alternative to local injections of the drugs, avoiding further pain and discomfort (You et al., 2017).

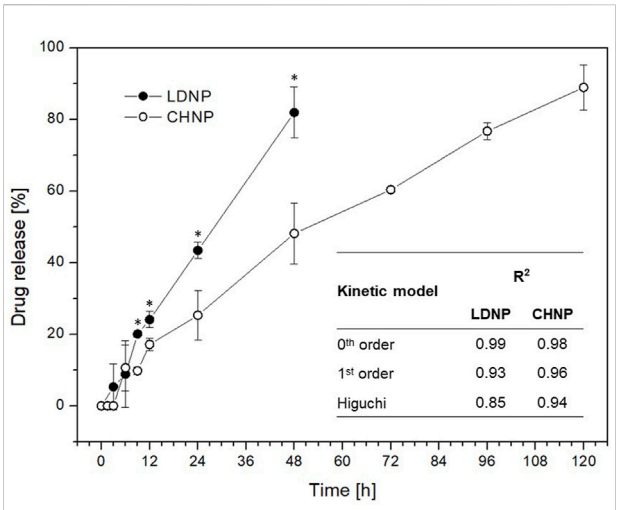

FIGURE 1
Drug release from nanoparticles. Lidocaine and chloramphenicol release profiles from lidocaine- and chloramphenicol-loaded polycaprolactone nanoparticles (LDNP and CHNP, respectively). Coefficients of determination (R^2) for three different fitting models: 0^{th} order, 1^{st} order, and Higuchi.

The analytical method for the simultaneous quantitation of both lidocaine and chloramphenicol was validated, showing selectivity, linearity within 0.5–50 μg/ml, precision (relative standard deviation, RSD < 5%), and accuracy (> 95%).

The drug encapsulation efficiencies (EE) were estimated at 77% for LDNP and 83% for CHNP, corresponding to about 4–5 mg of either lidocaine or chloramphenicol encapsulated in nanoparticles (Table 2). This amount of encapsulated lidocaine is expected to raise the intensity and the duration of the analgesia relatively to the free drug, besides reducing its local and systemic toxicities (Takenami et al., 2012; Ramos Campos et al., 2013). Similarly, this amount of encapsulated chloramphenicol is expected to improve the bactericidal effect relatively to the free drug, besides reducing its toxicity (Mandal et al., 2009; Soscia et al., 2010; Kalita et al., 2015; Kiruthika et al., 2015; Marslin et al., 2017).

Drug release reached about 80–90% after 48 h for LDNP and 120 h for CHNP (Figure 1). Quantifiable amounts of released drug were detected only after 3 h for lidocaine and after 6 h for chloramphenicol. Within 24 h, about 40% of lidocaine and 20% of chloramphenicol had been released, hence lidocaine is expected to be released faster than chloramphenicol.

LDNP data could be properly modeled by a typical 0^{th} order kinetics (constant drug release rate, R^2 = 0.99, Figure 1; Supplementary Figure S1). Within the assessed timeframe, CHNP data seemingly also follows a 0th order kinetics (R^2 = 0.98), although the experimental data could quite closely be modeled by a typical 1st order kinetics (drug release rate proportional to the remaining drug contents, R^2 = 0.96, Figure 1; Supplementary Figure S1). Assuming 0^{th} order kinetics for both LDNP and CHNP, their drug release rate would be, respectively, 2.18 ± 0.05 %/h and 0.98 ± 0.04 %/h (Supplementary Figure S1).

In a previous study, lidocaine release from PCL nanospheres was faster than the observed in the present study within the first 6 h (Ramos Campos et al., 2013). On the other hand, the release profile observed for chloramphenicol was very similar to the one reported by Kalita et al. (2015). The therapeutic effects of lidocaine are thus expected to act in combination with those of chloramphenicol, in a controlled and sustainable manner, as the biomembranes slowly degrade (Ma et al., 2016).

3.2 Preparation and characterization of drug-eluting chitosan/hyaluronic acid biomembranes

Dry weight, thickness, tensile strength (TS) and elongation at break (EB) for all the biomembranes prepared for this study are shown in Table 3. Overall, Group 2_{100} membranes exhibited higher mean dry weight compared to Group 1_{35} membranes. Their mean thickness varied within about 0.1–0.3 mm, with intragroup significant differences overall related to differences in designed glycerol (GL) contents (Table 1). The same trend was observed for both TS and EB values, suggesting that GL plays a significant role in their final mechanical properties. In general, the higher the GL contents, the higher the thickness, the lower the TS and the higher the EB observed (Tables 1, 3).

Indeed, GL has well-known plasticizing effects, endowing more flexibility and less mechanical resistance to polymeric matrices to which it is incorporated (Fundo et al., 2014; Ma et al., 2017). The increase in membrane thickness correlated to a higher amount of GL was also observed elsewhere (Mazzarino et al., 2014), being attributed to an increase in the separation in between polymeric chains due to GL.

With regards to their macroscopic aspect, the surface of membranes with lower amounts of HA were visually smoother and more homogeneous, as expected (Yao and Wu, 2011). By combining the positively charged CS chains with the negatively charged HA chains, the formation of a polyelectrolyte complex (PEC) is expected (Nath et al., 2015). The electrostatic interaction between the positive amines in CS and the negative carboxyl groups in HA were reported to be the strongest interaction within this PEC, and an increase in the amount of HA was correlated with an increase in macroscopic surface roughness (Vasile et al., 2013; Nath et al., 2015).

The surface and cross-sectional microscopic morphologies of selected membranes ($M1_{2.21}$ and $M2_{211}$), with and without embedded LDNP and CHNP, are shown on the scanning electron micrographs in Figure 2. Both the surface and the cross-sectional views of $M1_{2.21}$ and $M2_{211}$ are clearly rougher for samples with LDNP and CHNP. Round structures suggest the presence of nanoparticles, indicating that the embedding protocol was successful.

TABLE 3 Biomembranes: Physical and mechanical properties.

		Dry weight [mg/cm^2]	Thickness [mm]	TS [MPa]	EB [%]
Group 1_{35}	$M1_{221}$	23 ± 1^{d}	$0.10 \pm 0.04^{b,d}$	$1.4 \pm 0.4^{a,c,d}$	$49 \pm 12^{a,b}$
	$M1_{215}$	$48 \pm 4^{a,c,e}$	$0.14 \pm 0.02^{b,d}$	$0.7 \pm 0.2^{b,d}$	56 ± 4^{a}
	$M1_{2.21}$	20 ± 5^{d}	0.10 ± 0.02^{e}	$1.5 \pm 0.4^{a,c}$	40 ± 6^{a}
	$M1_{2.25}$	$46 \pm 10^{a,c,e}$	$0.13 \pm 0.03^{b,d,e}$	$0.7 \pm 0.1^{b,d}$	58 ± 3^{b}
Group 2_{100}	$M2_{221}$	56 ± 2^{a}	$0.18 \pm 0.04^{a,b}$	2.1 ± 0.4^{a}	$45 \pm 7^{a,b}$
	$M2_{215}$	87 ± 11^{b}	0.32 ± 0.07^{c}	$0.8 \pm 0.1^{b,c}$	$53 \pm 8^{a,b}$
	$M2_{2.21}$	42 ± 5^{c}	0.16 ± 0.02^{d}	2.0 ± 0.5^{a}	$49 \pm 4^{a,b}$
	$M2_{2.25}$	80 ± 5^{b}	0.23 ± 0.04^{a}	$1.1 \pm 0.2^{b,c}$	$53 \pm 9^{a,b}$

TS, tensile strength; **EB**, elongation at break; **M**, membrane. Different superscript letters indicate statistically significant differences ($p < 5\%$).

Figure 3A brings the *in vitro* degradation profiles of Group 1_{35} and Group 2_{100} membranes separately. Group 1_{35} membranes degraded faster than Group 2_{100} membranes. Seemingly, within each group, the higher the GL contents, the higher the degradation rate. Indeed, the separation in between polymeric chains promoted by GL was reported to speed up degradation. Although thicker, these membranes are more susceptible to swelling and degradation (Mazzarino et al., 2014). Particularly, $M1_{2.21}$ and $M2_{211}$ were more resistant to degradation in simulated saliva after 28 days and were then selected for the following characterizations/studies.

Figure 3B shows the swelling profiles for $M1_{2.21}$ and $M2_{211}$ membranes. After 15 min, $M2_{211}$ reached a mean swelling index (SI) plateau at about 150%. Comparatively, $M1_{2.21}$ reached an SI of approximately 330% in 15 min, then continued its hydration through the 24 h of study, up to a mean SI around 450%. Consistently, with a higher amount of GL, $M2_{211}$ was less susceptible to swelling than $M1_{2.21}$ (Mazzarino et al., 2014).

Figure 3C displays the drug release profiles for $M1_{2.21}$ and $M2_{211}$ membranes, embedded with LDNP and CHNP. During the first hour, we observe the so-called "burst effect", both for LDNP and CHNP. Following this initial fast release, a slow sustained release was verified up to the 24 h of observation. A similar behavior was highlighted for chitosan biomembranes in previous reports (Elgadir et al., 2015). The "burst effect" is generally associated to the release of drugs which were previously encapsulated close to the nanoparticles surface (Aminu et al., 2013). No significant differences were observed between the release profiles of $M1_{2.21}$ and $M2_{211}$, neither for LDNP nor for CHNP. Hence, membrane degradation and swelling profiles seem to prevail over LDNP and CHNP release profiles in terms of the overall drug release, as preconized by other authors for chitosan-based films (Ren et al., 2005; Labib et al., 2014) and observed for chloramphenicol- (Sanchez-Rexach et al., 2018) and lidocaine-loaded membranes (Thein-Han and Stevens, 2004).

Figure 3D summarizes the results obtained from the antibacterial activity assays. Following the CSLI standards (CLSI, 2018), if an inhibition halo with diameter greater than 18 mm is formed around chloramphenicol disks after 24 h of exposure, *S. aureus* can be considered "susceptible" to the antibiotic. If the halo diameter is in between 13–17 mm, its sensitivity is regarded as "intermediate". However, if the halo diameter is lower than 12 mm, *S. aureus* can be considered "resistant" to the antibiotic.

In our assays, chloramphenicol alone induced the formation of a 30-mm halo after 24 h of incubation with *S. aureus*, attesting its antibacterial activity (Figure 3D, top left). Similarly, when loaded with CHNP, both $M1_{2.21}$ and $M2_{211}$ ($^{+}M1_{2.21}$ and $^{+}M2_{211}$) induced the formation of 25-mm halos, suggesting that *S. aureus* can be inhibited by these membranes. When deprived of CHNP ($^{-}M1_{2.21}$ and $^{-}M2_{211}$), no inhibition halo was formed (Figure 3D, bottom left), which indicates that the antibacterial activity observed comes solely from chloramphenicol, and not from CS, HA, GL, or other membrane components.

Analogously, chloramphenicol alone induced the formation of a 50-mm halo after 24 h of incubation with *A. actinomycetemcomitans*, attesting its antibacterial activity (Figure 3D, top right). Likewise, $^{+}M1_{2.21}$ and $^{+}M2_{211}$ induced the formation of inhibition halos, suggesting that *A. actinomycetemcomitans* can be inhibited by these membranes. In turn, $^{-}M1_{2.21}$ and $^{-}M2_{211}$, both deprived of CHNP, did not induce inhibition halos (Figure 3D, bottom right).

Noteworthy, CS has been reported as an intrinsic bactericidal agent (Dash et al., 2011). Although controversial, its antibacterial activity is seemingly related to polymeric chains with high molecular weight and low acetylation (Kanwar et al., 2017). The CS used in this study had low molecular weight and, consistently with the literature, did not display perceivable bactericidal action.

The antibacterial activity of HA was reported to correlate with its concentration, molecular weight, functionalization, and

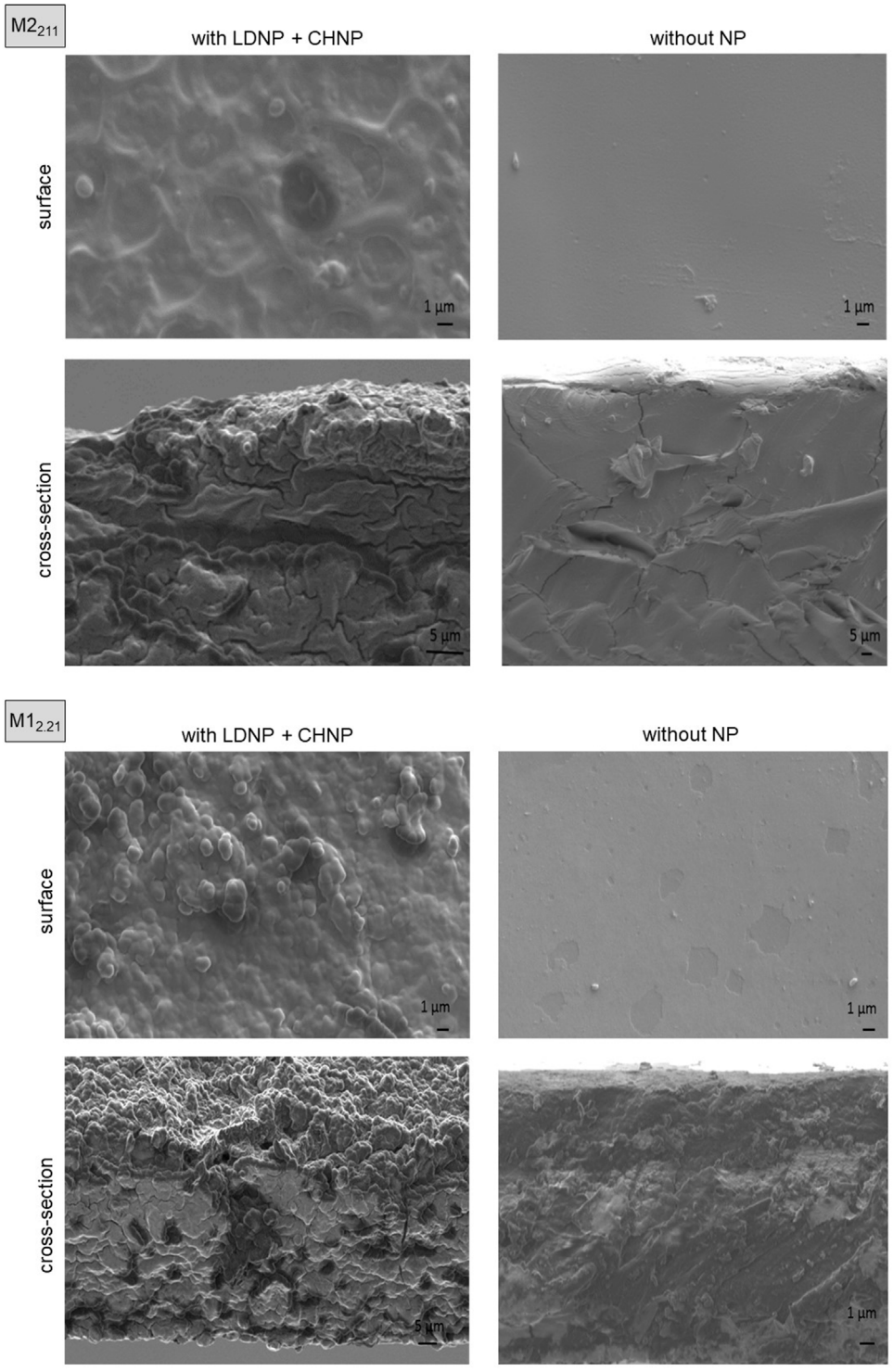

FIGURE 2
Biomembranes morphology. Surface and cross-sectional scanning electron micrographs taken from chitosan/hyaluronic acid/glycerol (CS/HA/GL) representative membranes $M1_{2.21}$ and $M2_{211}$, either with or without embedded LDNP and CHNP.

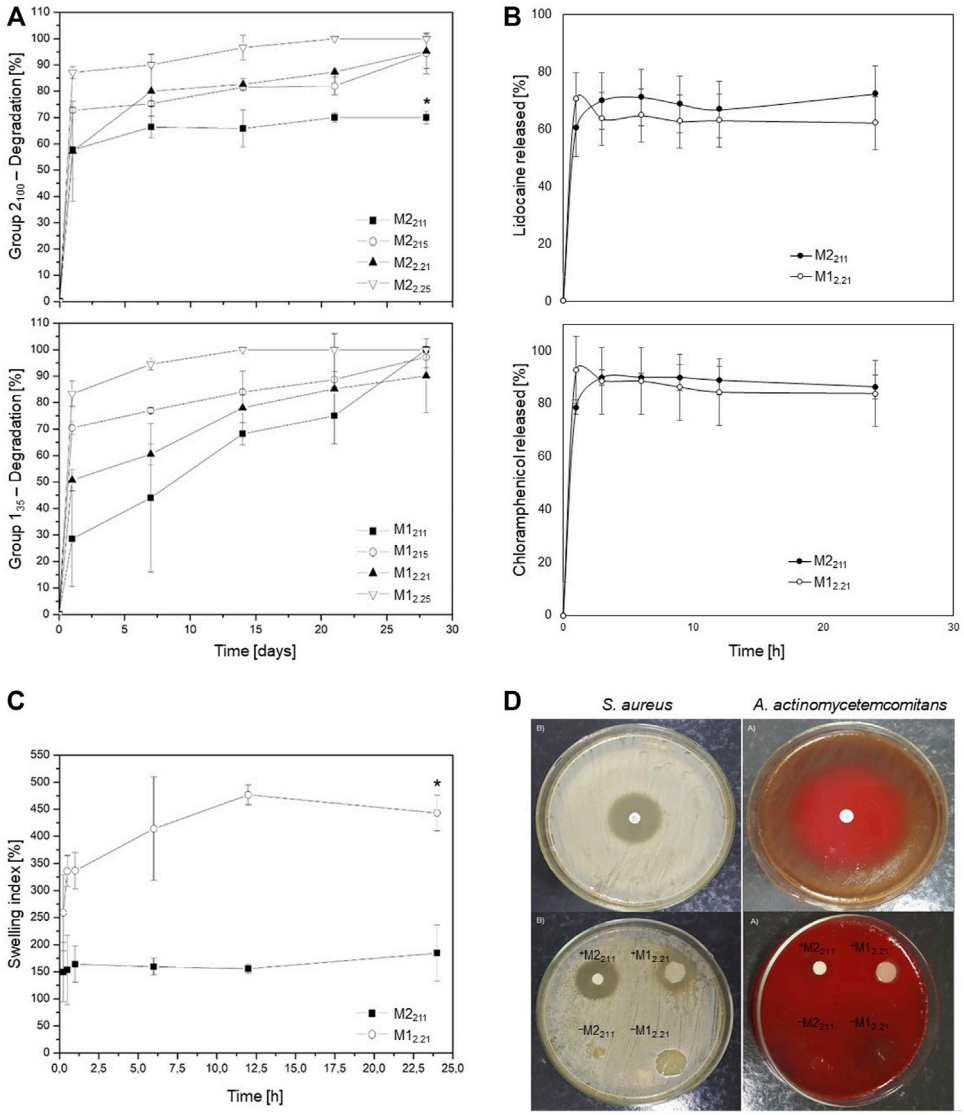

FIGURE 3
Biomembranes degradation, swelling, release kinetics, and antibacterial activity. **(A)** Degradation profiles of membranes incubated in simulated saliva. **(B)** Swelling profiles of membranes $M1_{2.21}$ and $M2_{211}$ in simulated saliva. **(C)** LDNP and CHNP release profiles from membranes $M1_{2.21}$ and $M2_{211}$. **(D)** Chloramphenicol (top), $M1_{2.21}$ and $M2_{211}$ (bottom) antibiotic activity against *S. aureus* and *A. actinomycetemcomitans*. The superscripts + and − indicate whether $M1_{2.21}$ and $M2_{211}$ were embedded or not with LDNP and CHNP.

bacterial strains assessed (Dahiya and Kamal, 2013; Lequeux et al., 2014; Romanò et al., 2017). At the concentrations used in this work, HA did not exhibit perceivable activity against the assessed strains.

Figure 4 shows the results of the biocompatibility tests. Green fluorescence (calcein staining) comes from viable cells, while red fluorescence (EthD-1 staining) comes from non-viable/dead cells.

No significant cytotoxicity was observed for $^{-}M2_{211}$ (not loaded with LDNP and CHNP), since cell viability remained at 99%, like the corresponding control. Slight cytotoxicity was observed in the vicinity of $^{+}M2_{211}$ (loaded with LDNP and CHNP), with cell viability reduced to 80%.

Unlike $M2_{211}$, $M1_{2.21}$ exhibited some cytotoxicity even when deprived of nanoparticles ($^{-}M1_{2.21}$), with cell viability reduced to 93%. Moreover, significant cytotoxicity was observed for $^{+}M1_{2.21}$, even at regions relatively distant from the vicinity of the membrane, the overall viability decreasing to 32%.

The results obtained for $M2_{211}$ are consistent with those observed by other authors in terms of the intrinsic toxicity of

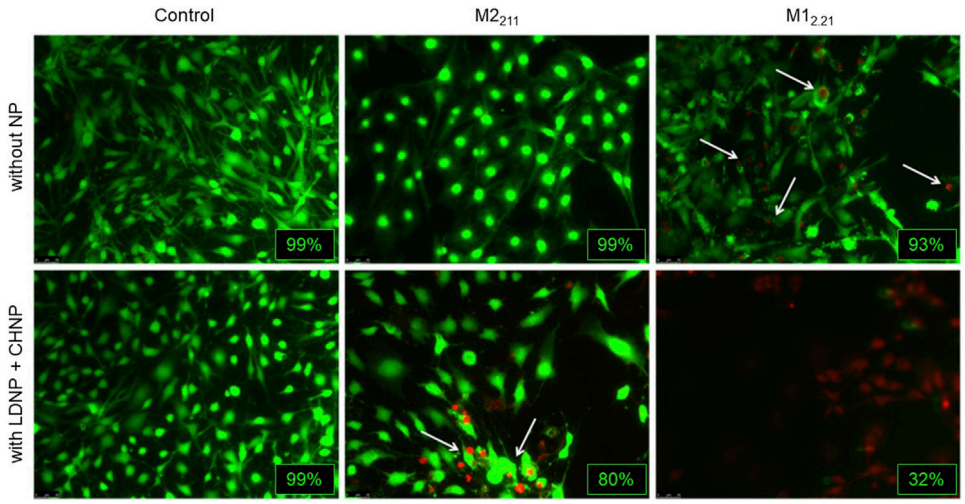

FIGURE 4
Biomembranes biocompatibility. Membranes $M1_{2.21}$ and $M2_{211}$ toxicity against 3T3 cells, either with or without embedded LDNP and CHNP. Green fluorescence (calcein staining) indicates viable cells, while red fluorescence (EthD-1 staining) indicates non-viable cells. Viabilities, calculated *via* Eqn 4, are shown for each image/sample.

chloramphenicol (Kostopoulou et al., 2015; Nada et al., 2016). On the other hand, the significantly higher cytotoxicity presented by $M1_{2.21}$ suggests that this biomembrane was unexpectedly intrinsically toxic.

4 Discussion

Drug-eluting biomembranes were obtained by the incorporation of lidocaine- and chloramphenicol-loaded polycaprolactone (PCL) nanoparticles (LDNP and CHNP, respectively) to a biodegradable polymeric matrix composed of chitosan (CS), hyaluronic acid (HA), and glycerol (GL) (Table 1).

LDNP and CHNP final size, polydispersion, encapsulation efficiencies (EE) and release profiles were shown to be suitable for the embedding, with similar total amounts of encapsulated drug (Table 2; Figure 1). Indeed, with sizes as small as 210 nm, the total surface area comprised by LDNP and CHNP tends to increase interactions and eventually binding between negatively charged ketones of their PCL structure to the structural components of the biomembranes, particularly to positively charged amines available in CS chains (Semnani et al., 2017; Kalantari et al., 2019). The reduced polydispersion is an indicative that these interactions are expected to occur nearly homogeneously across the biomembranes surface area.

Moreover, the relatively high EE allowed the encapsulation of approximately 4.5 mg of lidocaine and 5.0 mg of chloramphenicol in a 6-ml colloidal dispersion of LDNP and CHNP, respectively. This is a relatively large amount of encapsulated drug to be eventually incorporated to the biomembranes. Indeed, chloramphenicol minimum inhibitory concentrations MIC_{50} and MIC_{90} are reported to be, respectively, 3 mg/L and 8 mg/L (Sueke et al., 2010). The total amount of chloramphenicol encapsulated in a 6-ml dispersion of CHNP was 5.0 ± 0.3 mg, hence a final concentration slightly below the designed one (about 0.83 mg/ml, Tables 1, 2). As the chloramphenicol release rate from CHNP was estimated at 0.98 ± 0.04 %/h (Supplementary Figure S1), the CHNP dispersion would be able to release about 8.2 mg/L per hour, which is greater than the chloramphenicol MIC_{90}, and thus suitable for a sustained antibiotic activity. Indeed, even if about 60% of the CHNP are not ultimately embedded in the biomembranes, the delivery system will still be able to provide more than 3 mg/ml of chloramphenicol (MIC_{50}) per hour.

However, based on their drug release profiles (Figure 2), the anesthetic effect of lidocaine is expected to take place within the first 48 h (2 days), whereas the antibacterial effect of chloramphenicol would be active up to 120 h (5 days) after exposure to the biological medium (saliva). The difference between the release rates of lidocaine (2.18 ± 0.05 %/h, Supplementary Figure S1, 0th order) and chloramphenicol (0.98 ± 0.04 %/h, Supplementary Figure S1, 0th order) is especially important for the envisaged application. Indeed, a few hours after the biomembrane is implanted, the anesthetic effects of lidocaine on the local oral mucosa will be rapidly felt, relieving the patient from pain and discomfort (Ribeiro et al., 2016). On the other hand, the bactericidal activity of chloramphenicol is expected right after the biomembrane implantation, but also some time (days) after

the procedure, in order to prevent bacterial growth, diminishing the risk of infections (Tihan et al., 2015). Since 0^{th} order release kinetics seems appropriate for both drugs, we can expect these effects occurring at a constant rate during the whole timeframe of the treatment (guided tissue regeneration, GTR).

Membranes physicochemical and mechanical properties were noticeably dependent on their designed composition. GL clearly exerted greater influence on their dry weight, thickness, tensile strength (TS), and elongation at break (EB), which can be attributed to its well-known plasticizing function (Table 1 and Table 3). Overall, membranes with higher designed amounts of GL were the ones with greater dry weight, thickness, and EB (hence, lower TS). As a plasticizer, GL promotes the separation of adjacent polymer chains by reducing the intermolecular interactions within the polymeric network, resulting in loosening, greater matrix flexibility, and lower mechanical resistance (Fundo et al., 2014; Ma et al., 2017).

The incorporation of nanoparticles to biomembranes may modify their physicochemical/mechanical properties and morphology (Ng et al., 2013; Morihama and Mierzwa, 2014; Hasan et al., 2017). In this work, LDNP and CHNP did not significantly altered the physicochemical/mechanical properties of the developed membranes, although their morphology was clearly affected (Figure 2). Positively charged amines in CS chains strongly attract negatively charged functional groups (e.g., carboxyl and hydroxyl groups) in HA chains, leading to the formation of a polyelectrolyte complex (PEC), which serve as a scaffold for the embedding of drug-loaded NPs (Nath et al., 2015). The resulting polymeric matrix is expected to be dense, smooth, and homogeneous, as attested by surface and cross-sectional scanning electron micrographs of samples without nanoparticles in Figure 2.

Changes in the morphology, as those seen in samples with LDNP and CHNP in Figure 2, can be caused by various factors. One of the main challenges of the embedding process is to preserve the homogeneity of the original matrix. Indeed, even monodispersed nanoparticles can form aggregates when introduced to the polymeric matrix, as a result of interactions with its structural components (Kim et al., 2005). These aggregates may be due to the colloid original concentration, ionic strength, and pH, or may be related to the nanoparticle dimensions, morphology, and surface ligands, overall increasing/reducing physicochemical interactions with the polymeric network (Ng et al., 2013).

Importantly, the entrapment in polymeric matrices generally does not impair the nanoparticle designed functionality, the final delivery system benefiting both from the matrix physicochemical/mechanical properties and from the controlled/sustained drug release engendered by the embedded nanoparticles (Contri et al., 2014; Cardoso et al., 2019). Chitosan positive amines in the CS/HA/GL membranes are expected to attract polycaprolactone (PCL) negative ketones in LDNP and CHNP, favoring the embedding, an interaction widely explored for assembling electrospun nanofibers (Semnani et al., 2017; Kalantari et al., 2019). The resulting membrane roughness observed in Figure 2 is reported to foster the adhesion of biomolecules, consequently promoting cell adhesion and proliferation in guided tissue regeneration (GTR) applications (Ma et al., 2010; Cardoso et al., 2019).

Membranes degradation and swelling profiles in aqueous media are expected to be a function of the hydrophilic/hydrophobic nature of their structural components. Figure 3A suggests that GL-rich samples ($M1_{215}$ and $M1_{2.25}$ in Group 1_{35}, and $M2_{215}$ and $M2_{2.25}$ in Group 2_{100}) were less resistant to degradation in simulated saliva. In turn, Figure 3B indicates that $M2_{211}$ is less susceptible to swelling than $M1_{2.21}$.

Indeed, the amount of structural HA and GL determines the crosslinking degree within the polymeric network, with degradation being proportional to the number of free amines in CS chains and to the porosity of the matrix (Mathews et al., 2014). Moreover, the presence of polar groups, such as the hydroxyl and carboxyl groups in HA, are reported to favor water absorption and diffusion through a polymeric matrix (Silva, 2013; Tarusha et al., 2018). The higher the water absorption, the higher the swelling index and the higher the probability of hydrolysis, hence the higher the matrix degradation rate and consequent loss of the original physicochemical/mechanical properties (Kim et al., 2005).

The drug release profiles in Figure 3C could suggest that drug-elution from the CS/HA/GL matrix would be characterized by an initial burst-release followed by a slow sustained release. We highlight, however, that these profiles correspond to LDNP and CHNP release from the biomembranes, whereas the anesthetic effect of lidocaine and the antibacterial effect of chloramphenicol are expected to be a function of the release kinetics in Figure 1. Indeed, drug efficacy/toxicity is expected solely after its eventual release from the PCL nanoparticles towards the site of action (Gikas et al., 2004; Kotoky et al., 2015; Preem et al., 2017). Accordingly, LDNP and CHNP first detach from the biomembrane structures and then start the release of lidocaine and chloramphenicol, respectively. Indeed, the hydrolysis of the biomembrane structure, including the unbounding between PCL negative ketones (in LDNP and CHNP) and CS positive amines (of the biomembranes), is expected to precede the actual lidocaine and chloramphenicol co-release—which is, in turn, a result of the hydrolysis of the PCL structure of both LDNP and CHNP. Combined, the release profiles in Figures 1, 3C demonstrate that both $M1_{2.21}$ and $M2_{211}$ can provide the desirable therapeutic effects in a controlled and sustained manner.

For the antibacterial activity assays, *S. aureus* was chosen as a representative of gram-positive bacterial strains, whereas *A. actinomycetemcomitans* was selected as a representative of gram-negative bacterial strains (Tihan et al., 2015; Szafrański et al., 2017). Corroborating this drug-elution kinetics, the antibacterial activity of $M1_{2.21}$ and $M2_{211}$ could be successfully verified against both *S. aureus* and *A. actinomycetemcomitans* bacterial strains, as shown in Figure 3D. Indeed, inhibition halos induced by chloramphenicol alone (top) closely resemble those induced by the functionalized membranes (bottom, $^{+}M1_{2.21}$ and $^{+}M2_{211}$). No inhibition halo was induced by membranes deprived from CHNP (bottom, $^{-}M1_{2.21}$ and $^{-}M2_{211}$), which suggests that CS, HA, and GL, at the designed concentrations, have no significant antibacterial effects, although some toxicity has already been attributed intrinsically to CS (Dash et al., 2011). For instance, there are studies reporting that biomembranes composed exclusively by CS chains (with high molecular weight and low level of acetylation) were able to inhibit the action of *A. actinomycetemcomitans*—although no inhibition was observed for *S. aureus* (Kmiec et al., 2017; Ma et al., 2017). This might be related to the absence/presence of the cell wall protection, with high molecular weight positively charged CS chains with low level of acetylation more prone to interact and degrade negatively charged bacterial membranes deprived from cell wall protection (gram-negative).

Finally, $M1_{2.21}$ and $M2_{211}$ were submitted to biocompatibility assays (Figure 4), to evaluate their safety when in contact with mammalian cells, especially due to the intrinsic toxicity of chloramphenicol. The 3T3 murine lineage of fibroblasts was selected for this assay, since it is a common model of healthy mammalian cells (Henklewska et al., 2021). The greater cytotoxicity observed for $M1_{2.21}$ might not be related to its drug-release kinetics, since it is very similar to that of $M2_{211}$ (Figure 3C). Therefore, $M1_{2.21}$ cytotoxicity might be related to its degradation and swelling rates (Figures 3A,B), clearly higher than that of $M2_{211}$. Richer in HA, $M2_{211}$ might also have benefited from HA pro-adhesiveness and pro-cell-growth properties (Yamane et al., 2005; Schneider et al., 2007; Kaderli et al., 2015). Indeed, fibroblast growth and proliferation were reported to be a result of the modulation of the cellular microenvironment signaling due to the presence of HA (Chen et al., 2019).

5 Conclusion

Eight biomembranes, structurally composed by chitosan and hyaluronic acid polymeric chains, were developed, with mechanical properties, such as thickness, tensile strength, and elongation at break, modulated by the addition of glycerol as a plasticizing agent.

Lidocaine- and chloramphenicol-loaded nanoparticles were incorporated to the membranes, envisaging their application as drug-eluting systems in periodontal guided tissue regeneration. Two samples displayed greater resistance to degradation and swelling in simulated saliva and were then selected as optimal for further assays.

A burst release of lidocaine and chloramphenicol was observed for the membranes release profiles, which actually corresponds to the detachment of the drug-loaded nanoparticles. After detachment, a 0th order drug release kinetics is observed from the nanoparticles, with lidocaine being released almost 3 times faster than chloramphenicol. This controlled and sustainable drug release profile is notably due to the drug encapsulation in polycaprolactone nanoparticles.

Drug encapsulation efficiency was such that chloramphenicol minimum inhibitory concentration MIC_{50} per hour can be achieved even if the embedding efficiency is reduced to 40% only. As a result, the optimal samples exhibited bactericidal activity against both gram-positive *S. aureus* and gram-negative *A. actinomycetemcomitans* similar to the one observed for free chloramphenicol.

Richer in hyaluronic acid, one of these samples showed no intrinsic toxicity against 3T3 murine fibroblasts, a common model for healthy cells, and may now be further optimized as a drug-eluting biomembrane with potential for guided tissue regeneration.

Data availability statement

The raw data supporting the conclusions of this article will be made available by the authors, without undue reservation.

Author contributions

Conceptualization: MOV and EL. Methodology, formal analysis, and investigation: MOV, LS, TS, CS, ASJ, and EL. Writing-original draft preparation: LS and ASJ. Writing-review and editing: LS and EL. Supervision: LS and EL. Funding acquisition: MCV and EL. All authors have read and approved the final version of the manuscript.

Funding

This research was funded by the following Brazilian research funding agencies: Conselho Nacional de Desenvolvimento Científico e Tecnológico (CNPq), Financiadora de Estudos e Projetos (FINEP), Coordenação de Aperfeiçoamento de Pessoal de Nível Superior (CAPES), Fundação de Apoio à Pesquisa da Universidade Federal de Goiás (FUNAPE), and Fundação de Amparo à Pesquisa do Estado de Goiás (FAPEG).

Acknowledgments

The authors kindly thank Prof. Luís de Macêdo Farias, affiliated to the Department of Microbiology of the Institute of Biological Sciences at the Federal University of Minas Gerais (UFMG), for providing the bacterial strains used in this study.

Conflict of interest

The authors declare that the research was conducted in the absence of any commercial or financial relationships that could be construed as a potential conflict of interest.

Publisher's note

All claims expressed in this article are solely those of the authors and do not necessarily represent those of their affiliated organizations, or those of the publisher, the editors and the reviewers. Any product that may be evaluated in this article, or claim that may be made by its manufacturer, is not guaranteed or endorsed by the publisher.

Supplementary material

The Supplementary Material for this article can be found online at: https://www.frontiersin.org/articles/10.3389/fnano.2022.1049599/full#supplementary-material

References

Al-Rimawi, F., and Kharoaf, M. (2011). Analysis of chloramphenicol and its related compound 2-Amino-1-(4-nitrophenyl)propane-1, 3-diol by reversed-phase high-performance liquid chromatography with UV detection. *Chromatogr. Res. Int.* 2011, 1–6. doi:10.4061/2011/482308

Aminu, N., Baboota, S., Pramod, K., Singh, M., Dang, S., Ansari, S. H., et al. (2013). Development and evaluation of triclosan loaded poly-ε-caprolactone nanoparticulate system for the treatment of periodontal infections. *J. Nanopart. Res.* 15, 2075. doi:10.1007/s11051-013-2075-6

Anisha, B. S., Biswas, R., Chennazhi, K. P., and Jayakumar, R. (2013). Chitosan–hyaluronic acid/nano silver composite sponges for drug resistant bacteria infected diabetic wounds. *Int. J. Biol. Macromol.* 62, 310–320. doi:10.1016/j.ijbiomac.2013.09.011

Aravamudhan, A., Ramos, D. M., Nip, J., Harmon, M. D., James, R., Deng, M., et al. (2013). Cellulose and collagen derived micro-nano structured scaffolds for bone tissue engineering. *J. Biomed. Nanotechnol.* 9, 719–731. doi:10.1166/jbn.2013.1574

Ballini, A., Cantore, S., Capodiferro, S., and Grassi, F. R. (2009). Esterified hyaluronic acid and autologous bone in the surgical correction of the infra-bone defects. *Int. J. Med. Sci.* 6, 65–71. doi:10.7150/ijms.6.65

Battistella, E., Varoni, E., Cochis, A., Palazzo, B., and Rimondini, L. (2011). Degradable polymers may improve dental practice. *J. Appl. Biomater. Biomech.* 9, 223–231. doi:10.5301/JABB.2011.8867

Bhavsar, A. K., Parween, S., Karthikeyan, B. V., and Prabhuji, M. L. V. (2018). Critical issues in periodontal regeneration - a review. *J. Os. oral Heal. Dent. Sci.* 2, 1–8.

Bhusal, P., Sharma, M., Harrison, J., Procter, G., Andrews, G., Jones, D. S., et al. (2017). Development, validation and application of a stability indicating HPLC method to quantify lidocaine from polyethylene-co-vinyl acetate (EVA) matrices and biological fluids. *J. Chromatogr. Sci.* 55, 832–838. doi:10.1093/chromsci/bmx043

Cardoso, A. M., de Oliveira, E. G., Coradini, K., Bruinsmann, F. A., Aguirre, T., Lorenzoni, R., et al. (2019). Chitosan hydrogels containing nanoencapsulated phenytoin for cutaneous use: Skin permeation/penetration and efficacy in wound healing. *Mater. Sci. Eng. C* 96, 205–217. doi:10.1016/j.msec.2018.11.013

Castillo Dalí, G., and Torres Lagares, D. (2016). "Nanobiomaterials in hard tissue engineering," in *Nanobiomaterials in hard tissue engineering - applications of nanobiomaterials* (Amsterdam, Netherlands: Elsevier), 4, 1–31. doi:10.1016/B978-0-323-42862-0.00001-8

Chen, M., Li, L., Wang, Z., Li, P., Feng, F., and Zheng, X. (2019). High molecular weight hyaluronic acid regulates P. gingivalis–induced inflammation and migration in human gingival fibroblasts via MAPK and NF-κB signaling pathway. *Arch. Oral Biol.* 98, 75–80. doi:10.1016/j.archoralbio.2018.10.027

CLSI (2018). *Performance Standards for Antimicrobial Susceptibility Testing*. 28th Edn. Wayne, PA: Clinical and Laboratory Standards Institute CLSI supplement M100.

Contri, R. V., Katzer, T., Ourique, A. F., da Silva, A. L. M., Beck, R. C. R., Pohlmann, A. R., et al. (2014). Combined effect of polymeric nanocapsules and chitosan hydrogel on the increase of capsaicinoids adhesion to the skin surface. *J. Biomed. Nanotechnol.* 10, 820–830. doi:10.1166/jbn.2014.1752

Contri, R. V., Katzer, T., Pohlmann, A. R., and Guterres, S. S. (2010). Chitosan hydrogel containing capsaicinoids-loaded nanocapsules: An innovative formulation for topical delivery. *Soft Mat.* 8, 370–385. doi:10.1080/1539445X.2010.525161

Dahiya, P., and Kamal, R. (2013). Hyaluronic acid: A boon in periodontal therapy. *N. Am. J. Med. Sci.* 5, 309. doi:10.4103/1947-2714.112473

Dash, M., Chiellini, F., Ottenbrite, R. M., and Chiellini, E. (2011). Chitosan—a versatile semi-synthetic polymer in biomedical applications. *Prog. Polym. Sci.* 36, 981–1014. doi:10.1016/j.progpolymsci.2011.02.001

Elgadir, M. A., Uddin, M. S., Ferdosh, S., Adam, A., Chowdhury, A. J. K., and Sarker, M. Z. I. (2015). Impact of chitosan composites and chitosan nanoparticle composites on various drug delivery systems: A review. *J. Food Drug Anal.* 23, 619–629. doi:10.1016/j.jfda.2014.10.008

Fessi, H., Puisieux, F., Devissaguet, J. P., Ammoury, N., and Benita, S. (1989). Nanocapsule formation by interfacial polymer deposition following solvent displacement. *Int. J. Pharm. X.* 55, R1–R4. doi:10.1016/0378-5173(89)90281-0

Fundo, J. F., Fernandes, R., Almeida, P. M., Carvalho, A., Feio, G., Silva, C. L. M., et al. (2014). Molecular mobility, composition and structure analysis in glycerol plasticised chitosan films. *Food Chem. x.* 144, 2–8. doi:10.1016/j.foodchem.2013.05.127

Gikas, E., Kormali, P., Tsipi, D., and Tsarbopoulos, A. (2004). Development of a rapid and sensitive SPE-LC-ESI MS/MS method for the determination of chloramphenicol in seafood. *J. Agric. Food Chem.* 52, 1025–1030. doi:10.1021/jf030485l

Gupta, K. C., and Ravi Kumar, M. N. V. (2000). Drug release behavior of beads and microgranules of chitosan. *Biomaterials* 21, 1115–1119. doi:10.1016/S0142-9612(99)00263-X

Hasan, S., Thomas, N., Thierry, B., and Prestidge, C. (2017). Controlled and localized nitric oxide precursor delivery from chitosan gels to *Staphylococcus aureus* biofilms. *J. Pharm. Sci.* 106, 3556–3563. doi:10.1016/j.xphs.2017.08.006

Henklewska, M., Pawlak, A., Li, R.-F., Yi, J., Zbyryt, I., and Obmińska-Mrukowicz, B. (2021). Benzyl isothiocyanate, a vegetable-derived compound, induces apoptosis via ROS accumulation and DNA damage in canine lymphoma and leukemia cells. *Int. J. Mol. Sci.* 22, 11772. doi:10.3390/ijms222111772

Ionta, F. Q., Mendonça, F. L., de Oliveira, G. C., de Alencar, C. R. B., Honório, H. M., Magalhães, A. C., et al. (2014). *In vitro* assessment of artificial saliva formulations on initial enamel erosion remineralization. *J. Dent. (Shiraz).* 42, 175–179. doi:10.1016/j.jdent.2013.11.009

Iqbal, M. S., Shad, M. A., Ashraf, M. W., Bilal, M., and Saeed, M. (2006). Development and validation of an HPLC method for the determination of dexamethasone, dexamethasone sodium phosphate and chloramphenicol in

presence of each other in pharmaceutical preparations. *Chromatographia* 64, 219–222. doi:10.1365/s10337-006-0019-3

Kaderli, S., Boulocher, C., Pillet, E., Watrelot-Virieux, D., Rougemont, A. L., Roger, T., et al. (2015). A novel biocompatible hyaluronic acid-chitosan hybrid hydrogel for osteoarthrosis therapy. *Int. J. Pharm. X.* 483, 158–168. doi:10.1016/j.ijpharm.2015.01.052

Kalantari, K., Afifi, A. M., Jahangirian, H., and Webster, T. J. (2019). Biomedical applications of chitosan electrospun nanofibers as a green polymer – Review. *Carbohydr. Polym.* 207, 588–600. doi:10.1016/j.carbpol.2018.12.011

Kalita, S., Devi, B., Kandimalla, R., Sharma, K. K., Sharma, A., Kalita, K., et al. (2015). Chloramphenicol encapsulated in poly-ε-caprolactone-pluronic composite: Nanoparticles for treatment of MRSA-infected burn wounds. *Int. J. Nanomedicine* 10, 2971–2984. doi:10.2147/IJN.S75023

Kanwar, I., Sah, A. K., and Suresh, P. K. (2017). Biofilm-mediated antibiotic-resistant oral bacterial infections: Mechanism and combat strategies. *Curr. Pharm. Des.* 23, 2084–2095. doi:10.2174/1381612822666161124154549

Khorsand, B., Elangovan, S., Hong, L., Kormann, M. S. D., and Salem, A. K. (2019). A bioactive collagen membrane that enhances bone regeneration. *J. Biomed. Mat. Res.* 107, 1824–1832. doi:10.1002/jbm.b.34275

Kim, S., Nimni, M. E., Yang, Z., and Han, B. (2005). Chitosan/gelatin-based films crosslinked by proanthocyanidin. *J. Biomed. Mat. Res.* 75B, 442–450. doi:10.1002/jbm.b.30324

Kiruthika, V., Maya, S., Suresh, M. K., Anil Kumar, V., Jayakumar, R., and Biswas, R. (2015). Comparative efficacy of chloramphenicol loaded chondroitin sulfate and dextran sulfate nanoparticles to treat intracellular Salmonella infections. *Colloids Surfaces B Biointerfaces* 127, 33–40. doi:10.1016/j.colsurfb.2015.01.012

Kmiec, M., Pighinelli, L., Tedesco, M. F., Silva, M. M., and Reis, V. (2017). Chitosan-properties and applications in dentistry. *Adv. Tissue Eng. Regen. Med. Open Access* 2, 205–211. doi:10.15406/atroa.2017.02.00035

Kostopoulou, O. N., Magoulas, G. E., Papadopoulos, G. E., Mouzaki, A., Dinos, G. P., Papaioannou, D., et al. (2015). Synthesis and evaluation of chloramphenicol homodimers: Molecular target, antimicrobial activity, and toxicity against human cells. *PLoS One* 10, e0134526. doi:10.1371/journal.pone.0134526

Kotoky, J., Kandimalla, R., Kalita, S., Devi, B., Sharma, K. K., Sharma, A., et al. (2015). Chloramphenicol encapsulated in poly-ε-caprolactone-pluronic composite: Nanoparticles for treatment of MRSA-infected burn wounds. *Int. J. Nanomedicine* 2971, 2971–2984. doi:10.2147/IJN.S75023

Labib, G. S., Aldawsari, H. M., and Badr-Eldin, S. M. (2014). Metronidazole and pentoxifylline films for the local treatment of chronic periodontal pockets: Preparation, *in vitro* evaluation and clinical assessment. *Expert Opin. Drug Deliv.* 11, 855–865. doi:10.1517/17425247.2014.897325

Lequeux, I., Ducasse, E., Jouenne, T., and Thebault, P. (2014). Addition of antimicrobial properties to hyaluronic acid by grafting of antimicrobial peptide. *Eur. Polym. J.* 51, 182–190. doi:10.1016/j.eurpolymj.2013.11.012

Ma, J., Zhang, M., Jiang, Z., Nie, M., and Liu, G. (2010). Facile fabrication of structurally stable hyaluronic acid-based composite membranes inspired by bioadhesion. *J. Memb. Sci.* 364, 290–297. doi:10.1016/j.memsci.2010.08.027

Ma, S., Adayi, A., Liu, Z., Li, M., Wu, M., Xiao, L., et al. (2016). Asymmetric collagen/chitosan membrane containing minocycline-loaded chitosan nanoparticles for guided bone regeneration. *Sci. Rep.* 6, 31822. doi:10.1038/srep31822

Ma, S., Chen, Z., Qiao, F., Sun, Y., Yang, X., Deng, X., et al. (2014). Guided bone regeneration with tripolyphosphate cross-linked asymmetric chitosan membrane. *J. Dent. (Shiraz).* 42, 1603–1612. doi:10.1016/j.jdent.2014.08.015

Ma, Y., Xin, L., Tan, H., Fan, M., Li, J., Jia, Y., et al. (2017). Chitosan membrane dressings toughened by glycerol to load antibacterial drugs for wound healing. *Mater. Sci. Eng. C* 81, 522–531. doi:10.1016/j.msec.2017.08.052

Mandal, B., Halder, K. K., Dey, S. K., Bhoumik, M., Debnath, M. C., and Ghosh, L. K. (2009). Development and physical characterization of chloramphenicol loaded biodegradable nanoparticles for prolonged release. *Pharmazie* 64, 445–449. doi:10.1691/ph.2009.8274

Marslin, G., Liu, X., Xiaolei, S., and Xiang, W. (2017). PEG-PLGA nanoencapsulation improves the antibacterial activity of chloramphenicol. *Lat. Am. J. Pharm.* 36, 2001–2006.

Mathews, S., Bhonde, R., Gupta, P. K., and Totey, S. (2014). Novel biomimetic tripolymer scaffolds consisting of chitosan, collagen type 1, and hyaluronic acid for bone marrow-derived human mesenchymal stem cells-based bone tissue engineering. *J. Biomed. Mat. Res.* 102, 1825–1834. doi:10.1002/jbm.b.33152

Mazzarino, L., Borsali, R., and Lemos-Senna, E. (2014). Mucoadhesive films containing chitosan-coated nanoparticles: A new strategy for buccal curcumin release. *J. Pharm. Sci.* 103, 3764–3771. doi:10.1002/jps.24142

Morihama, A. C. D., and Mierzwa, J. C. (2014). Clay nanoparticles effects on performance and morphology of poly(vinylidene fluoride) membranes. *Braz. J. Chem. Eng.* 31, 79–93. doi:10.1590/S0104-66322014000100009

Nada, A. A., Montaser, A. S., Abdel Azeem, R. A., and Mounier, M. M. (2016). Eco-friendly gelatin-based electrospun fibers to control the release of chloramphenicol. *Fibers Polym.* 17, 1985–1994. doi:10.1007/s12221-016-6596-3

Nath, S. D., Abueva, C., Kim, B., and Lee, B. T. (2015). Chitosan–hyaluronic acid polyelectrolyte complex scaffold crosslinked with genipin for immobilization and controlled release of BMP-2. *Carbohydr. Polym.* 115, 160–169. doi:10.1016/j.carbpol.2014.08.077

Ng, Y. L., Mohammad, A. W., Leo, C. P., and Hilal, N. (2013). Polymeric membranes incorporated with metal/metal oxide nanoparticles : A comprehensive review. *Desalination* 308, 15–33. doi:10.1016/j.desal.2010.11.033

Osathanon, T., Chanjavanakul, P., Kongdecha, P., Clayhan, P., and Huynh, N. C.-N. (2017). "Polycaprolactone-based biomaterials for guided tissue regeneration membrane," in *Periodontitis - a useful reference* (Rang-Du-Fliers, France: InTech). doi:10.5772/intechopen.69153

Patel, V. F., Liu, F., and Brown, M. B. (2011). Advances in oral transmucosal drug delivery. *J. Control. Release* 153, 106–116. doi:10.1016/j.jconrel.2011.01.027

Prado-Prone, G., Silva-Bermudez, P., Bazzar, M., Focarete, M. L., Rodil, S. E., Vidal-Gutiérrez, X., et al. (2020). Antibacterial composite membranes of polycaprolactone/gelatin loaded with zinc oxide nanoparticles for guided tissue regeneration. *Biomed. Mat.* 15, 035006. doi:10.1088/1748-605X/ab70ef

Pramod, K., Aji Alex, M. R., Singh, M., Dang, S., Ansari, S. H., and Ali, J. (2016). Eugenol nanocapsule for enhanced therapeutic activity against periodontal infections. *J. Drug Target.* 24, 24–33. doi:10.3109/1061186X.2015.1052071

Preem, L., Mahmoudzadeh, M., Putrinš, M., Meos, A., Laidmäe, I., Romann, T., et al. (2017). Interactions between chloramphenicol, carrier polymers, and bacteria–implications for designing electrospun drug delivery systems countering wound infection. *Mol. Pharm.* 14, 4417–4430. doi:10.1021/acs.molpharmaceut.7b00524

Ramos Campos, E. V., Silva de Melo, N. F., Guilherme, V. A., de Paula, E., Rosa, A. H., de Araújo, D. R., et al. (2013). Preparation and characterization of poly(ε-caprolactone) nanospheres containing the local anesthetic lidocaine. *J. Pharm. Sci.* 102, 215–226. doi:10.1002/jps.23350

Ren, D., Yi, H., Wang, W., and Ma, X. (2005). The enzymatic degradation and swelling properties of chitosan matrices with different degrees of N-acetylation. *Carbohydr. Res.* 340, 2403–2410. doi:10.1016/j.carres.2005.07.022

Ribeiro, L. N. M., Franz-Montan, M., Breitkreitz, M. C., Alcântara, A. C. S., Castro, S. R., Guilherme, V. A., et al. (2016). Nanostructured lipid carriers as robust systems for topical lidocaine-prilocaine release in dentistry. *Eur. J. Pharm. Sci.* 93, 192–202. doi:10.1016/j.ejps.2016.08.030

Romanò, C. L., De Vecchi, E., Bortolin, M., Morelli, I., and Drago, L. (2017). Hyaluronic acid and its composites as a local antimicrobial/antiadhesive barrier. *J. Bone Jt. Infect.* 2, 63–72. doi:10.7150/jbji.17705

Sanchez-Rexach, E., Meaurio, E., Iturri, J., Toca-Herrera, J. L., Nir, S., Reches, M., et al. (2018). Miscibility, interactions and antimicrobial activity of poly(ε-caprolactone)/chloramphenicol blends. *Eur. Polym. J.* 102, 30–37. doi:10.1016/j.eurpolymj.2018.03.011

Schneider, A., Richert, L., Francius, G., Voegel, J.-C., and Picart, C. (2007). Elasticity, biodegradability and cell adhesive properties of chitosan/hyaluronan multilayer films. *Biomed. Mat.* 2, S45–S51. doi:10.1088/1748-6041/2/1/S07

Semnani, D., Naghashzargar, E., Hadjianfar, M., Dehghan Manshadi, F., Mohammadi, S., Karbasi, S., et al. (2017). Evaluation of PCL/chitosan electrospun nanofibers for liver tissue engineering. *Int. J. Polym. Mater. Polym. Biomaterials* 66, 149–157. doi:10.1080/00914037.2016.1190931

Sgorla, D., Almeida, A., Azevedo, C., Bunhak, É. J., Sarmento, B., and Cavalcanti, O. A. (2016). Development and characterization of crosslinked hyaluronic acid polymeric films for use in coating processes. *Int. J. Pharm. X.* 511, 380–389. doi:10.1016/j.ijpharm.2016.07.033

Shi, R., Ye, J., Li, W., Zhang, J., Li, J., Wu, C., et al. (2019). Infection-responsive electrospun nanofiber mat for antibacterial guided tissue regeneration membrane. *Mater. Sci. Eng. C* 100, 523–534. doi:10.1016/j.msec.2019.03.039

Silva, M. S. (2013). *Análise bioquímica e funcional de bandagem bucal antimicrobiana*, Master of Science—Dissertation. Bauru: University of São Paulo. doi:10.11606/D.25.2013.tde-14102013-153219

Soscia, D. A., Raof, N. A., Xie, Y., Cady, N. C., and Gadre, A. P. (2010). Antibiotic-loaded PLGA nanofibers for wound healing applications. *Adv. Eng. Mat.* 12, B83–B88. doi:10.1002/adem.200980016

Sueke, H., Kaye, S., Neal, T., Murphy, C., Hall, A., Whittaker, D., et al. (2010). Minimum inhibitory concentrations of standard and novel antimicrobials for isolates from bacterial keratitis. *Invest. Ophthalmol. Vis. Sci.* 51, 2519. doi:10.1167/iovs.09-4638

Szafrański, S. P., Deng, Z.-L., Tomasch, J., Jarek, M., Bhuju, S., Rohde, M., et al. (2017). Quorum sensing of Streptococcus mutans is activated by Aggregatibacter actinomycetemcomitans and by the periodontal microbiome. *BMC Genomics* 18, 238. doi:10.1186/s12864-017-3618-5

Takenami, T., Wang, G., Nara, Y., Fukushima, S., Yagishita, S., Hiruma, H., et al. (2012). Intrathecally administered ropivacaine is less neurotoxic than procaine, bupivacaine, and levobupivacaine in a rat spinal model. *Can. J. Anesth/J. Can. Anesth.* 59, 456–465. doi:10.1007/s12630-012-9685-9

Tarusha, L., Paoletti, S., Travan, A., and Marsich, E. (2018). Alginate membranes loaded with hyaluronic acid and silver nanoparticles to foster tissue healing and to control bacterial contamination of non-healing wounds. *J. Mat. Sci. Mat. Med.* 29, 22. doi:10.1007/s10856-018-6027-7

Thein-Han, W. W., and Stevens, W. F. (2004). Transdermal delivery controlled by a chitosan membrane. *Drug Dev. Ind. Pharm.* 30, 397–404. doi:10.1081/DDC-120030934

Tihan, G. T., Ungureanu, C., Constantin Barbaresso, R., Gabriela Zgârian, R., Rău, I., Meghea, A., et al. (2015). Chloramphenicol collagen sponges for local drug delivery in dentistry. *C. R. Chim.* 18, 986–992. doi:10.1016/j.crci.2015.06.004

Vahabi, S., and Mardanifar, F. (2014). Applications of Nanotechnology in dentistry: A review. *J. Dent. Sch.* 32, 228–239. doi:10.22037/jds.v32i4.24781

Vasile, C., Pieptu, D., Dumitriu, R. P., Pânzariu, A., and Profire, L. (2013). Chitosan/hyaluronic acid polyelectrolyte complex hydrogels in the management of burn wounds. *Rev. Med. Chir. Soc. Med. Nat. Iasi* 117, 565–571.

Wang, S., and Jing, Y. (2017). Study on the barrier properties of glycerol to chitosan coating layer. *Mat. Lett.* 209, 345–348. doi:10.1016/j.matlet.2017.08.040

Xu, C., Cao, Y., Lei, C., Li, Z., Kumeria, T., Meka, A. K., et al. (2020). Polymer–mesoporous silica nanoparticle core–shell nanofibers as a dual-drug-delivery system for guided tissue regeneration. *ACS Appl. Nano Mat.* 3, 1457–1467. doi:10.1021/acsanm.9b02298

Xu, H., Ma, L., Shi, H., Gao, C., and Han, C. (2007). Chitosan–hyaluronic acid hybrid film as a novel wound dressing: *In vitro* and *in vivo* studies. *Polym. Adv. Technol.* 17, 869–875. doi:10.1002/pat.906

Yamane, S., Iwasaki, N., Majima, T., Funakoshi, T., Masuko, T., Harada, K., et al. (2005). Feasibility of chitosan-based hyaluronic acid hybrid biomaterial for a novel scaffold in cartilage tissue engineering. *Biomaterials* 26, 611–619. doi:10.1016/j.biomaterials.2004.03.013

Yan, X., Khor, E., and Lim, L.-Y. (2000). PEC films prepared from chitosan-alginate coacervates. *Chem. Pharm. Bull.* 48, 941–946. doi:10.1248/cpb.48.941

Yao, Z.-A., and Wu, H.-G. (2011). Characterization of chitosan-hyaluronic acid blended membranes and their effects on the growth of keratocytes. *Polym. Polym. Compos.* 19, 573–580. doi:10.1177/096739111101900707

Yin, I. X., Zhang, J., Zhao, I. S., Mei, M. L., Li, Q., and Chu, C. H. (2020). The antibacterial mechanism of silver nanoparticles and its application in dentistry. *Int. J. Nanomedicine* 15, 2555–2562. doi:10.2147/IJN.S246764

You, P., Yuan, R., and Chen, C. (2017). Design and evaluation of lidocaine-and prilocaine-coloaded nanoparticulate drug delivery systems for topical anesthetic analgesic therapy: A comparison between solid lipid nanoparticles and nanostructured lipid carriers. *Drug Des. devel. Ther.* 11, 2743–2752. doi:10.2147/DDDT.S141031

Zhang, E., Zhu, C., Yang, J., Sun, H., Zhang, X., Li, S., et al. (2016). Electrospun PDLLA/PLGA composite membranes for potential application in guided tissue regeneration. *Mater. Sci. Eng. C* 58, 278–285. doi:10.1016/j.msec.2015.08.032

Zhang, N., Xiao, F., Bai, J., Lai, Y., Hou, J., Xian, Y., et al. (2011). Label-free immunoassay for chloramphenicol based on hollow gold nanospheres/chitosan composite. *Talanta* 87, 100–105. doi:10.1016/j.talanta.2011.07.108